

Article

Endurance of Polymeric Insulation Foil Exposed to DC-Biased Medium-Frequency Rectangular Pulse Voltage Stress

Raphael Färber ^{1,*}, Thomas Guillod ², Florian Krismer ², Johann W. Kolar ² and Christian M. Franck ¹

¹ High Voltage Laboratory (HVL), Department of Information Technology and Electrical Engineering, ETH Zürich, 8092 Zürich, Switzerland; cfranck@ethz.ch

² Power Electronic Systems Laboratory (PES), Department of Information Technology and Electrical Engineering, ETH Zürich, 8092 Zürich, Switzerland; guillod@lem.ee.ethz.ch (T.G.); krismer@lem.ee.ethz.ch (F.K.); kolar@lem.ee.ethz.ch (J.W.K.)

* Correspondence: faerberr@ethz.ch

Received: 27 November 2019; Accepted: 13 December 2019; Published: 18 December 2019



Abstract: The endurance of polymeric insulation foil is investigated under a mixed medium-voltage stress (DC + medium-frequency rectangular pulse) by means of accelerated lifetime testing. A dedicated setup is used that allows us to selectively eliminate the known risk factors for premature insulation failure under medium-frequency pulse voltage stress: partial discharges (PDs) during pulse transitions, excessive dielectric heating, and systemic overvoltages. The obtained results on polyethylenterephthalat (PET) insulation foil suggest that the adequate consideration of these factors is *sufficient* for eliminating the adverse effects of the pulse modulation under the investigated conditions. Indeed, if all mentioned risk factors are eliminated, the time to failure observed under a pure DC stress is *shorter* than with a superimposed pulse (keeping the same peak voltage). There is then no indication of an additional detrimental “per pulse” degradation process (i.e., the time to failure is not dependent on pulse frequency). In contrast, when repetitive PDs are present, the lifetime under combined DC + rectangular pulse stress strongly decreases with increasing pulse switching frequency. PD erosion of the foil is quantified by means of confocal microscopy, and the applicability of the streamer criterion for predicting PD inception is discussed.

Keywords: dry-type insulation; aging; time to failure; partial discharge; power electronics; inverter; converter; medium-frequency; pulse-width-modulated (PWM); electromechanical stress

1. Introduction

Medium voltage (MV, ≥ 1 kV) power electronic converters based on medium-frequency (MF, ≥ 1 kHz) energy conversion have stimulated numerous research efforts over the last years [1]. These converters, sometimes called Electronic Transformers or Solid State Transformers, use semiconductor switches to interface a power grid with a load or generator via a MF MV transformer (and other passive components). They thereby provide a galvanically isolated interface with controllable electric power flow between grids, loads, and generators of different voltage levels and frequencies (including DC). By employing switching frequencies of several kilohertz and beyond, these converters achieve significantly higher power densities (at equal efficiency) than their low-frequency (50 Hz) counterparts because the magnetic components scale approximately with the inverse of their operating frequency [1]. For these reasons, MV Electronic Transformers are expected to play a key role where actively controlled medium-voltage electrical energy conversion (AC-AC, AC-DC, DC-DC) is

needed, or when space/weight constraints apply, such as in medium-voltage electric mobility and electric aircraft applications [2].

The maturing of wide band gap semiconductor technologies for power switching applications (SiC and GaN) considerably enlarges the design space for MF MV converters. In particular, switching losses can be reduced significantly by the increased switching speeds ($>10\text{ kV}/\mu\text{s}$) [3], and a further increase in conversion power density is possible by increasing the switching frequency (up to and beyond 100 kHz).

Increased switching speeds and frequencies, however, raise issues concerning the long-term endurance of organic insulation materials employed in MV converter systems [4,5]. The accelerated degradation and premature failure of insulation systems exposed to inverter-type medium voltages in the presence of partial discharge (PD) is a largely investigated topic [6–10], and PD is recognized as one of the main risk factors associated with this type of voltage stress:

- a. *Enhanced partial discharge (PD) intensity.* The number of PDs per unit of time is proportional to the switching frequency. In addition, PD amplitudes are observed to increase with switching speed [11]. Thus, if PD is incepted, the total PD charge and its erosive effect on the insulation material is greatly enhanced when switching frequency and speed are increased.

Moreover, it has been recognized early on [12] that the waveform and fundamental frequency of the voltage influence the (local) electric field stress to which the insulation materials are subjected. Thus, this constitutes another risk factor that must be considered when dealing with inverter-type voltages:

- b. *Systemic overvoltages.* The broad spectral content of the terminal voltage can excite system resonances, generate standing wave phenomena on electrically long conductors (cable/load impedance mismatch), and lead to strongly nonlinear voltage drops along windings or field-grading layers due to parasitic capacitive couplings [4]. As a result, the electric field stress on certain parts of the insulation can be increased significantly.

While premature failure under inverter-type voltages in the absence of PD is also documented in literature [13,14], the investigation of the associated (accelerated) aging mechanism(s) has not received as much attention as PD degradation under these voltage profiles. The negative impact of increased insulation temperature due to enhanced dielectric losses [15] is often cited as a possible cause for premature insulation failure under repetitive pulse stress in the absence of PD [7,9,10,16] and is certainly a risk factor to be considered in the insulation design:

- c. *Excessive insulation temperature.* Increased switching speeds broaden the spectral content of the terminal voltage, while a higher switching frequency shifts its frequency spectrum as a whole. Both effects typically entail enhanced dielectric losses. Losses associated with charge migration or the dielectric α -relaxation have positive temperature coefficients and can lead to thermal runaway [17]. Moreover, increased capacitive currents can lead to significant heating of (field-grading) semiconductive layers [4]. Even in the absence of thermal runaway, a higher insulation temperature due to increased power (loss) densities enhances thermally activated degradation processes and—especially for organic materials—compromised (di)electric properties. Moreover, the problem of stress cracking and delamination is accentuated.

It has been shown [18] that (bulk) space charge evolves under inverter-type voltages that possess a DC offset (e.g., unipolar rectangular voltages). Thus, in addition to increased dielectric heating, several investigators also mention the possibility of space charge playing a role in premature failure, in particular, under DC-biased repetitive pulse voltages [19,20]. While it is well known that the distortion of the electrode field by space charges in the insulation bulk plays a key role under DC voltage stress [21], it remains unclear if the interaction of the highly dynamic electrode field with bulk

space charge influences insulation aging, because the available studies do not allow to clearly separate the influence of dielectric losses from the potential influence of space charge. A further potential aging mechanism is thus proposed and its relevance for insulation failure under DC-biased repetitive pulse voltage stress investigated in this work:

- d. *Space charge*. Structural aging due to electromechanical stress from the Coulombic interaction between the highly dynamic electrode field (due to repetitive impulse voltages of high slew rate) with space charge evolving under the DC-component of the applied voltage.

The concept that the interaction of space charge with the electrode field and the associated electromechanical stress can lead to the aging of polymeric (especially semicrystalline) insulation materials is not new. The electromechanical force density $f = \rho E$ (electrostriction omitted) acting on space charge is indeed a fundamental ingredient in several well-established microphysical models of dielectric aging, see [22–25]. While initially developed for DC voltage stress, the operant microphysical aging process (morphological changes such as the opening of sub-microvoids and crack propagation) can also be considered under AC or mixed (DC+AC) voltages. In this case, the deformation of the polymer structure (e.g., straining of polymer ties in the amorphous regions) will be modulated by the dynamics of the AC component of the electric field. It is argued in [26] (Chapter 6.6) that cyclic mechanical stress is expected to accelerate these processes because it causes the polymer chains to occupy conformational states that are more varied relative to the quasi-equilibrium states occupied under a constant electric field stress. Moreover, there is an additional mechanical energy dissipation (proportional to the excitation frequency) associated with the cyclic conformational changes.

It is thus expected that this mode of dielectric aging—if active at all—should be particularly pronounced when a DC voltage (promoting the creation of space charge) is modulated by a highly dynamic inverter-type voltage (i.e., with steep voltage fronts). At present, there is no lifetime data available in the literature on strictly unipolar repetitive impulse voltages that could help decide whether or not such an effect should be added to the list of risk factors when dealing with mixed voltages. Thus, in order to test this hypothesis, electrical endurance testing of polyethyleneterephthalat (PET) insulation foils is performed under a DC medium-voltage stress superimposed by medium-frequency rectangular voltage impulses (Figure 1c). A dedicated setup is used which allows us to eliminate the known risk factors b. (overstressing due to voltage overshoot) and c. (excessive heating of the sample), as well as to study the transition from the PD-free to the PD regime (risk factor a.). The aim of this investigation is thus to contribute to an empirical basis that helps to decide on the question of completeness of the listed risk factors a. to c. for arbitrary inverter-type voltages.

2. Methods

2.1. Test Bench

The simplified schematic of the MF pulse voltage generator (with variable DC-bias) constructed for the tests reported in this work is shown in Figure 1a. The pulse voltage is generated by a MOSFET half-bridge S_1/S_2 (Behlke HTS 21-07-HB-C) connected to the DC-bus capacitor $C_1 = 1 \mu\text{F}$ and superimposed onto the DC voltage by capacitive coupling through $C_2 = 2.7 \text{ nF}$. The DC voltage is applied to the sample through the $R_4 = 1 \text{ M}\Omega$ resistor, which provides the necessary decoupling of the DC voltage source. Due to the AC-coupling, the DC component of the voltage U_{DUT} is still given by U_{DC} . Choosing $C_2 \gg C_{\text{DUT}}$ ensures that most of the pulse voltage U_p drops across the specimen capacitance C_{DUT} (test cell and voltage probe capacitance are understood to be included in the latter). The resistors $R_2 = 220 \Omega$ and $R_3 \geq 50 \Omega$ along with the diodes D_1 and D_2 serve to protect the half-bridge in case of specimen breakdown ($U_{\text{DUT}} \rightarrow 0$). The value of R_3 can be increased to decrease the slew rate of the pulse voltage fronts. The maximal slew rate (at $R_3 = 50 \Omega$) is about $30 \text{ kV}/\mu\text{s}$.

In operation, the DC voltage U_{DC} drops across C_2 , and thus the output node of the half-bridge is pulled towards $\mp U_{\text{DC}}$ when the sample breaks down. The fast SiC diodes clamp this voltage rise by

providing a discharge path for C_2 through $C_2-R_3-D_2-R_{BD}$ (for $U_{DC} > 0$) or $C_2-R_3-D_1-C_1-R_{BD}$ (for $U_{DC} < 0$), where R_{BD} is the breakdown impedance of the specimen. R_2 reduces the share of the breakdown current carried by the MOSFET body diodes. A current monitor (CT) detects this discharge current, blocks S_1 and S_2 , and shuts down both voltage sources.

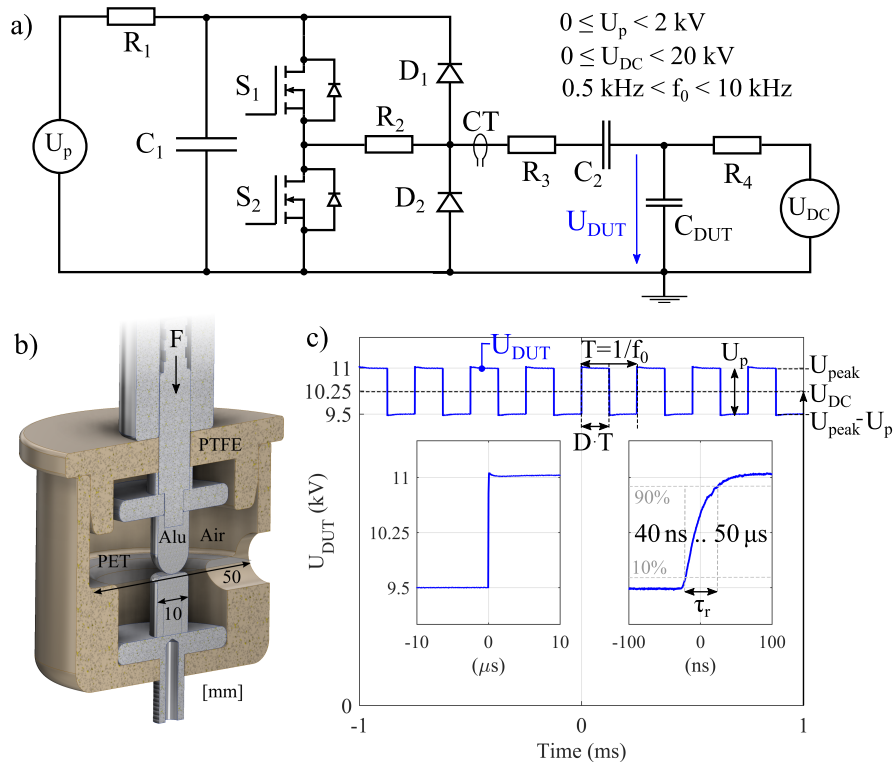


Figure 1. (a) Schematic of mixed-frequency (DC + AC pulse) voltage generator; (b) electrode-specimen geometry; (c) exemplary pulse voltage waveform used for time-to-failure testing of polyethylenterephthalat (PET) foil in this study.

2.2. Sample Preparation and Electrode Geometry

Polyethylenterephthalat (PET) insulation foil (DuPont Melinex[®] S) is used for the voltage endurance tests. It is a semicrystalline polymer foil, commonly used in electrical applications as a capacitor dielectric or as a layer insulation in high-voltage transformers. The idea was to use a “typical, widely used” insulation material such that the obtained results are more likely to be representative for a larger group of polymeric insulation materials. The nominal thickness of the used foil is $d = 23 \mu\text{m}$, and measured to be within $22.5 \mu\text{m}$ and $23.5 \mu\text{m}$ for all samples (all from the same reel). The foil is cut into circles of 50 mm diameter and stored in an air atmosphere with $(33 \pm 2)\%$ RH and a temperature of $22 \pm 2 \text{ }^\circ\text{C}$ for at least 12 h prior to testing. Before the sample is placed in the sample holder, shown in Figure 1b, its surface is cleaned with ethanol and possible static charges are removed by contacting both sides with a conductive foil. The sample holder is then placed inside the test cell, which is at room temperature $24 \pm 2 \text{ }^\circ\text{C}$. A strong dependence of the time to failure on the air relative humidity (RH) was observed (not further investigated in this study). The RH inside the test chamber was thus held constant at $(33 \pm 2)\%$ by a conditioned air purge flow ($\sim 10 \text{ L min}^{-1}$). At room temperature, the ingress of water molecules into a PET foil of $23 \mu\text{m}$ thickness is expected to reach the equilibrium concentration after a few minutes (estimation based on the diffusion length $2\sqrt{D \cdot t}$ and the diffusion constant $D = 4 \times 10^{-9} \text{ cm}^2 \text{ s}^{-1}$ [27]). Controlling the RH inside the test cell is thus important when testing thin dielectric samples.

The high-voltage electrode (lower electrode in Figure 1b) is planar (diameter 10 mm with 1.5 mm fillet radius) while the ground electrode is a half-sphere of radius 5 mm . A spring mechanism

generates a mechanical contact force $F_c \approx 3\text{ N}$ to ensure a reliable and reproducible electrode contact. The electrostatic force between the electrode charges leads to an additional, voltage-dependent contribution to the contact force. From the Hertzian theory of elastic contact [28], with the extension proposed in [29] to include thin sheets of elastic materials on a rigid substrate (see Appendix A), the foil indentation depth is calculated to be $\delta \approx 1.2\ \mu\text{m}$ at 11 kV ($\delta \approx 0.9\ \mu\text{m}$ at 0 kV), which corresponds to about 5% of the foil thickness. The target insulation volume is thus localized underneath the indent of diameter $2r_c = 2\sqrt{R\delta} \approx 0.16\ \text{mm}$. The foil is thus stressed with a quasi-homogeneous electrical field whose maximum is at the point of maximal indentation.

Outside of the indented region (near the triple point), the electrode potential is transferred to the polymer surface by means of partial discharges (PDs). If the repetitive pulses do not incept PDs, only the time-averaged voltage (i.e., the DC component) is transferred to the foil surface. Since all breakdown channels were located within the indented area, no attempt was made to quantify the lateral extent of the deposited surface charge layer.

The aluminum electrodes are removed and polished to a surface roughness of about $R_a \approx 0.44\ \mu\text{m}$ ($R_q \approx 0.58\ \mu\text{m}$) after each breakdown in order to eliminate the influence of metal protrusions generated by the breakdown channel. The surface roughness was estimated by means of confocal microscopy according to the international standard ISO 4287 (with Gaussian filter standard deviation $2.5\ \mu\text{m}$).

The PD inception voltage of the used electrode-specimen configuration is experimentally determined to lie between 1.0 and 1.1 kV. The sharp transition between the PD and non-PD regime can be well distinguished by means of an installed near-UV camera ($\sim 350\ \text{nm}$ to $\sim 380\ \text{nm}$) and a photomultiplier tube ($\sim 200\ \text{nm}$ to $\sim 380\ \text{nm}$). The inception voltage for repetitive PDs is determined only by the peak-to-peak value U_p of the pulse voltage, but not the DC-bias U_{DC} . Indeed, the latter is eliminated within the air gap by an initial deposition of surface charges near the electrode contact area on the foil. The repetition rate of PDs due to DC stressing (i.e., not caused by the voltage transitions of the pulse modulation) is measured to be below $1\ \text{s}^{-1}$ and its effect on insulation deterioration can thus be neglected (validated by microscopic inspection of the foil surface after stressing).

The described electrode-specimen configuration was chosen for the following reasons:

- The stressed volume is small, which allows to avoid a significant heating of the insulation even at high pulse frequencies (quantitative analysis given in Section 2.2.3), and thus to investigate insulation failure outside the thermal aging/thermal breakdown regime;
- The configuration has a high degree of (macroscopic) symmetry, and thus is more easily amenable to numerical estimations of system properties (thermal, electric field, etc.) than more complicated systems (such as twisted enamelled wires);
- The arrangement can be used to investigate the breakdown of polymeric insulation in the presence or absence of PDs without the need for replacing the surrounding air with insulating oil. This is a consequence of the well-defined insulator-electrode configuration and the associated existence of a narrowly scattered value of the inception voltage.

2.2.1. Test Procedure

The investigated voltage waveforms consist of a rectangular pulse train with a DC offset, as exemplified in Figure 1c. The test variable of main interest is the fundamental frequency f_0 of the pulse modulation. The pulse amplitude U_p is also varied in order to study the transition from the PD-free to the PD regime. The pulse duty cycle D and the pulse rise/fall time τ_r are kept at 0.5 and 40 ns, respectively, for all measurements presented here.

The DC offset voltage U_{DC} is adjusted to keep the nominal peak voltage at 11 kV for all tested values of pulse amplitudes U_p (transient overvoltages are quantified in Section 3.2). The nominal peak voltage is given by

$$U_{\text{peak}} = U_{DC} + U_p(1 - D) = U_{DC} + \frac{U_p}{2} \stackrel{!}{=} 11\ \text{kV} \quad \text{for all } U_p \ (D = 0.5). \quad (1)$$

As mentioned at the end of the Introduction, the prime motivation for choosing this type of mixed-voltage stress (DC + repetitive pulse) is the provision of favorable conditions for the occurrence of the hypothesized additional “per pulse” aging mechanism (d.), such that its impact on insulation lifetime can be assessed empirically. In addition, lifetime data on insulation aging under this voltage profile is of direct practical interest for the high-voltage insulation design of Input Series Output Parallel (ISOP) DC-DC converters [30], gate drive auxiliary transformers of MV solid-state switches, as well as MV power module insulation.

At the beginning of a test, the pulse voltage is applied and the DC bias is ramped up to its final value within five seconds. This stress is then left unchanged until breakdown occurs. The time to failure is recorded automatically when the breakdown current detector triggers. All samples are visually inspected to ensure the presence of the breakdown puncture.

2.2.2. Statistical Analysis

The recorded time-to-failure (TTF) values are fitted by a two-parameter Weibull distribution, whose cumulative distribution function is given by

$$F(\text{TTF}) = 1 - e^{-\left(\frac{\text{TTF}}{\alpha}\right)^\beta}. \quad (2)$$

The fit is obtained by performing a least-square linear regression in the coordinate system within which all Weibull distributions appear as straight lines (see Figure 2). It is obtained by plotting $\ln\{-\ln[1 - F(\text{TTF})]\}$ as a function of $\ln(\text{TTF})$.

The scale parameter α is equal to the 0.63 percentile, while the shape parameter β is a measure of the scatter of the TTF values around the median and is given by the slope of the regression line. Instead of the scale parameter, the 0.5 percentile (i.e., the median) will be used for the characteristic TTF values reported in the Results section. The 95% confidence interval for the median is obtained from the corresponding confidence bounds on the linear regression (the curved lines in Figure 2).

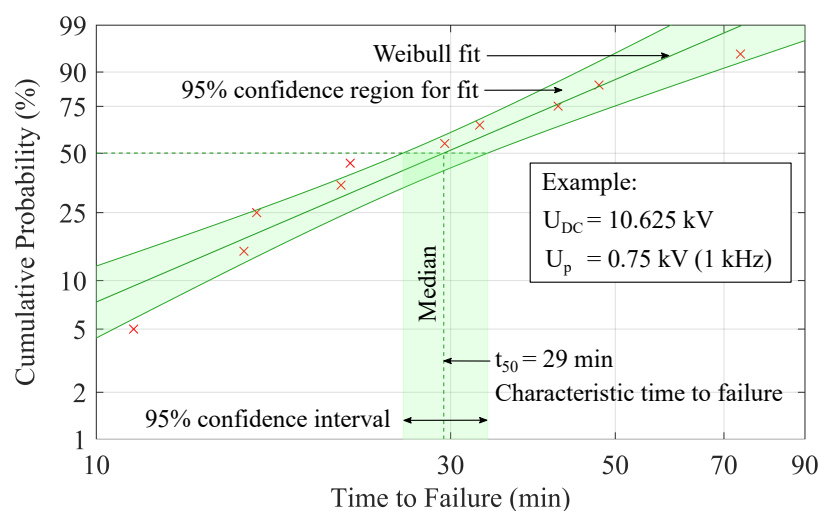


Figure 2. Ten times to failure are recorded for each stress condition and fitted by a Weibull distribution. The corresponding median value and its 95% confidence bound are given in Section 3.

2.2.3. Maximal Sample Temperature

Although the present study is designed to *not* operate in a regime where the polarization losses due to the pulse voltage cause a significant insulation temperature rise, dielectric heating of the foil was analyzed in detail in order to ensure that this is indeed the case.

Details on the the derivation of the following expressions are given in Appendix B. For an excitation voltage of period T ,

$$u(t) = \operatorname{Re} \left[\sum_{n=1}^{\infty} \underline{U}_n e^{j\omega_n t} \right] \quad \text{with } \omega_n = n \frac{2\pi}{T}, \quad (3)$$

an upper bound on the maximal insulation temperature is shown to be the solution of the iterative scheme

$$\vartheta_{i+1} = \vartheta_i + \frac{\dot{q}(\vartheta_i)}{\Gamma} \quad i = 1, 2, \dots, \quad (4)$$

where the (local) cooling coefficient Γ ($\text{W K}^{-1} \text{m}^{-3}$) is a function of the geometry, the thermal conductivity of the foil, and the thermal resistance to the heat bath of temperature ϑ_0 (electrodes). The spatial maximum of the dielectric loss density (W m^{-3} , time-averaged over a period T) is given by

$$\dot{q}(\vartheta) = \kappa_{\text{DC}}(\vartheta) \left[\frac{U_{\text{DC}}}{d} \right]^2 + \frac{\varepsilon_0}{2} \sum_{n=0}^{\infty} \omega_n \varepsilon''_{\text{eff},n}(\vartheta) \left[\frac{|U_n|}{d} \right]^2, \quad (5)$$

where κ_{DC} is the DC conductivity and $\varepsilon''_{\text{eff},n}$ is the imaginary part of the effective dielectric permittivity (it includes the DC conductivity for the voltage components $n \geq 1$).

3. Results

The results section starts out by showing that excessive insulation temperature can be excluded as a cause of insulation failure for the stress profiles and electrode configuration used in this study. Then, the measured characteristic TTF values (median and 95% confidence interval of the fitted Weibull distribution) are presented. It is shown that above a threshold value of the pulse modulation amplitude, repetitive PDs are present on the foil surface, leading to an insulation lifetime that decreases with increasing switching frequency. On the contrary, below PD inception (and in the absence of excessive dielectric heating as well as significant overvoltage), no accelerating influence of the switching transitions on insulation aging is observed.

3.1. Dielectric Heating

For (mixed) broadband voltages, the dielectric loss density is a convolution of the power spectrum and dielectric parameters, as given by Equation (5). For the numerical calculations, the effective dielectric permittivity $\varepsilon''_{\text{eff}}(\omega, \vartheta)$ was determined by dielectric spectroscopy on the actual PET foil samples used in the TTF testing. The following temperature parametrization of the DC conductivity of PET is used:

$$\kappa_{\text{DC}}(\vartheta) = \kappa_0 e^{-\frac{E_a}{k_B \vartheta}}, \quad (6)$$

where $\kappa_0 = 1.04 \cdot 10^5 \text{ S m}^{-1}$ and $E_a = 0.97 \text{ eV}$ are derived from the high-field measurement data (up to 50 kV mm^{-1}) provided in [31] by linear extrapolation to the maximal DC field strengths occurring here ($\sim 400 \text{ kV mm}^{-1}$). The maximum insulation temperature ϑ_m is determined with the formalism outlined in Section 2.2.3, by using worst-case estimates of the involved parameters (e.g., thermal coupling to electrodes). Of all the parameter combinations used in this study, the highest insulation temperature increase $\Delta\vartheta_m = \vartheta_m - \vartheta_0$ is obtained with $U_p = 1.5 \text{ kV}$, $f_0 = 8 \text{ kHz}$, $\tau_r = 40 \text{ ns}$, and equals about 3°C . The conduction losses (first term in Equation (5)) are negligible at room temperature and cannot be activated by the temperature rise provoked by the AC dielectric losses. Based on this analysis, it is thus justified to exclude risk factor c. (Excessive insulation temperature) as a plausible cause of insulation failure in this study.

With a view to the typically more bulky insulation encountered in actual MV insulation systems, it is useful to keep in mind that the risk of a thermal instability (at fixed electric field stress) increases rapidly with insulation thickness d , because the cooling coefficient Γ scales approximately as d^{-2} (see Appendix B, Equation (A19)). Moreover, the external losses from windings, magnetic core,

semiconductors, etc. add to the increase in insulation temperature and feature positive temperature coefficients, thereby contributing to the risk of thermal insulation failure.

3.2. Systemic Overvoltages

Repetitive systemic overvoltages occurring at the switching transition are identified as a risk factor for accelerated insulation aging under inverter-type voltages (risk factor b. mentioned in the Introduction). It is therefore important to quantify the actual voltage overshoot present in the system used for insulation testing, because the actual repetitive peak voltage can be significantly higher than the nominal peak voltage derived from the DC link capacitor voltage U_p (see Equation (1)). In this study, the combination of a low sample capacitance (<100 pF, including voltage probe and test cell parasitics) and low-inductive connections from the inverter output to the sample provides a negligible voltage overshoot (<5%) even at the shortest rise time ($\tau_r = 40$ ns). Above $\tau_r = 1$ μ s, the overshoot is below 1%. Measurements of the output waveform were performed with a LeCroy PPE 20 kV/100 MHz high-voltage probe.

3.3. Partial Discharge Inception Voltage (PDIV)

The partial discharge inception voltage of the employed electrode-specimen configuration is experimentally determined to lie between $U_p = 1$ kV and $U_p = 1.1$ kV (for a duty cycle $D = 0.5$ and hence $|U_{peak}| = U_{DC} + U_p/2$). The DC voltage component U_{DC} does not significantly influence the repetitive PDIV, since the associated component of the electric field is expelled from the air gap by an initial deposition of surface charges.

The presence of repetitive PDs leads to an erosion of the foil surface and a substantial reduction of the foil thickness. Figure 3a shows a confocal microscope image of the eroded area. The ring-shaped form of the eroded area is explained by the streamer criterion [32],

$$\int_0^{x_{crit}} \alpha_{eff}(x) dx \geq K_{St}, \quad (7)$$

which states that the integral of the effective ionization coefficient α_{eff} along a field line from the electrode surface ($x = 0$) to the edge of critical volume ($x = x_{crit}$) must exceed a certain threshold value known as the streamer constant K_{St} . The critical volume is the volume in which the effective ionization coefficient is positive, i.e., where electron avalanches can develop.

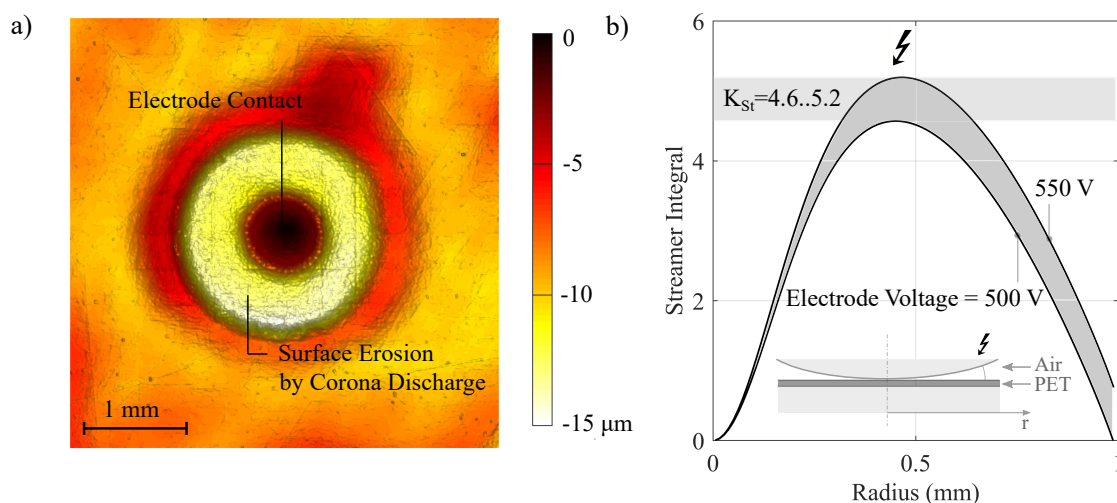


Figure 3. (a) Confocal microscope image of PD-eroded foil surface and (b) streamer integral value for electrode voltages as a function of the radial base point position of the electric field line.

By using the parametrization of α_{eff} provided in [33], the streamer integral for the investigated geometry features a maximum value at $r = r_{\text{max}} \approx 0.5$ mm, which agrees well with the measured erosion profile (Figure 3a). For $r \ll r_{\text{max}}$, the integration path within the air gap is too short for a streamer discharge to develop, while at $r \gg r_{\text{max}}$, the electric field along the field line is too weak to promote collision ionization. The value of the streamer constant predicting the observed PDIV lies in the range $4.6 < K_{\text{St}} < 5.2$.

3.4. Times to Failure

The time to failure as a function of the pulse amplitude U_p is shown in Figure 4. The peak voltage is kept at 11 kV. The switching frequency and the pulse rise/fall time are 4 kHz and 40 ns, respectively. It can be seen that the function $\text{TTF}(U_p)$ presents a maximum around the PDIV. At $U_p = 1$ kV the scatter is relatively larger, because some samples initiate PDs (with a corresponding lifetime shorter than for $U_p = 0.75$ kV) while others do not (with a lifetime longer than for $U_p = 0.75$ kV).

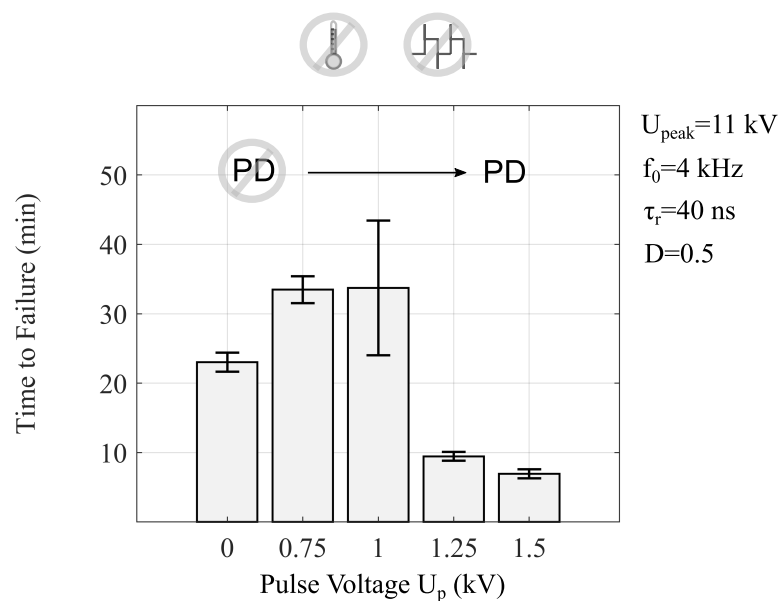


Figure 4. Below partial discharge inception voltage (PDIV) ($U_p < 1$ kV), the time to failure increases with increasing pulse voltage U_p (at fixed peak voltage $U_{\text{peak}} = 11$ kV). Above PDIV ($U_p > 1$ kV), on the other hand, the lifetime decreases with increasing pulse voltage amplitude.

The times to failure scale very differently as a function of switching frequency f_0 in the PD and PD-free regime. Figure 5a shows that there is a clear “per pulse” degradation in the presence of PDs ($U_p = 1.5$ kV). Quantitatively, the functional dependence $\text{TTF} \propto f_0^{-0.65}$ is obtained by a least square polynomial fit, which indicates that the deterioration per pulse decreases with increasing switching frequency.

A completely different picture is observed when the pulses are unable to incept PDs ($U_p = 0.75$ kV). As is shown in Figure 5b, the time to failure in this case is independent of the switching frequency (within statistical uncertainty), that is, $\text{TTF} \propto f_0^0$. Moreover, the measured value of the time to failure is about 30% larger on average than for a pure DC voltage of the same peak value.

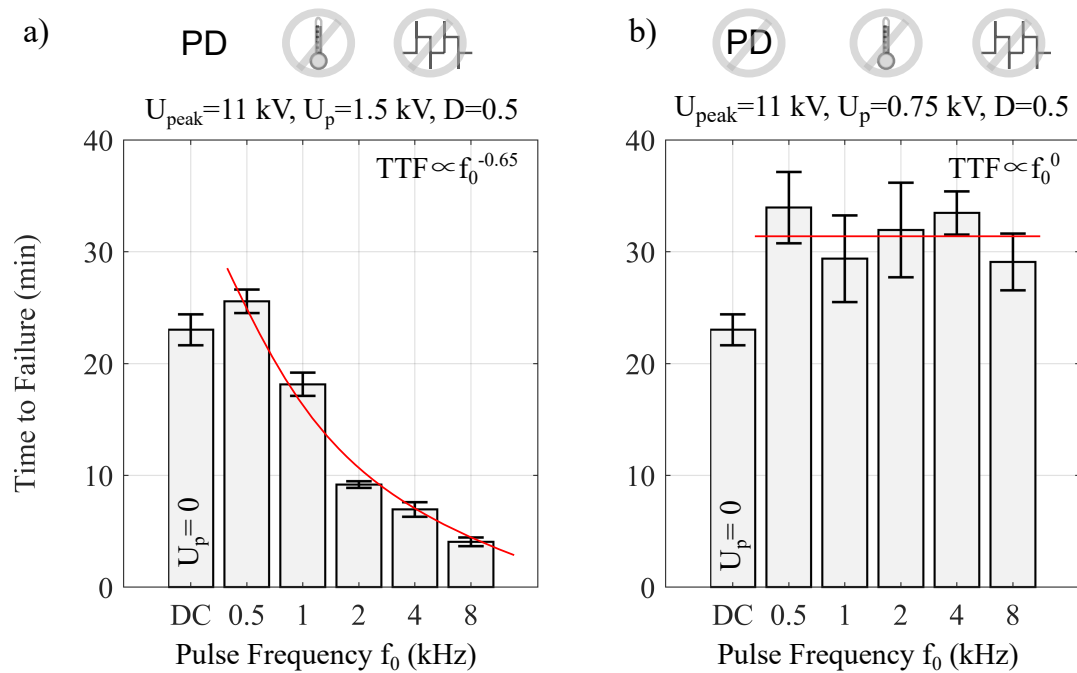


Figure 5. Characteristic times to failure (median of the fitted Weibull distribution) under DC-biased pulse voltages as a function of pulse fundamental frequency: (a) A “per pulse” degradation is active when the pulse modulation is able to inception repetitive PDs. (b) On the contrary, in the absence of PD (as well as transient overvoltages and excessive dielectric heating), the measured insulation lifetime is not significantly dependent on the pulse frequency, and *increased* compared to a pure DC voltage of the same peak value. The fitted curves illustrate the calculated power function dependency of the characteristic time to failure on pulse frequency.

4. Discussion

Before entering into the discussion of the results, it seems appropriate to stress that the conclusions drawn from the empirical data of this study should not be transferred to other types of mixed-voltage stresses and other insulation systems—unless there is a physical reason to do so. Moreover, it is important to be aware of the inherent limitations of accelerated aging tests, e.g., that the relative importance of different aging mechanisms can change as a function of the applied stress level. Moreover, in actual insulation systems, other types of insulation stressors (e.g., mechanical and environmental) are present and need to be addressed for reliable insulation designs.

The main goal of this study was to find out if there is experimental evidence of an additional degradation/aging mechanism (d.) that is activated by superimposing a repetitive pulse voltage onto a DC bias voltage. The risk factors b. (Transient overvoltage) c. (Excessive insulation temperature) are excluded in this study.

Repetitive PDs occur when the pulse amplitude exceeds a certain threshold value, and their presence results in a drastic decrease of insulation lifetime with increasing switching frequency. This reduction in lifetime can be explained by the erosive effect of the PDs: confocal microscopy of the foil surface shows that polymer material is removed below the dielectric barrier discharge plasma to a substantial fraction of the foil thickness. This leads to a steady increase in the electric field stress in the remaining layer of insulation, until its breakdown strength is exceeded. The lifetime under varying pulse fundamental frequencies scales inversely with the average intensity of the light emission captured by the near-UV camera. This is in line with the previous conclusion of PD erosion being the culprit for faster insulation deterioration for increased pulse repetition frequencies.

The spatial extent of the PD region agrees well with mathematical modeling based on the streamer criterion. However, the obtained value of the streamer constant K_5 predicting the observed value

of the PDIV is much lower ($K_S = 4.6...5.2$) than the standard value $K_S = 14...18$ traditionally used for determining streamer inception in air [34]. Similar low values ($K_{St} \approx 6$) of the streamer constant are reported in the recent literature [35] on the investigation of PDIV for twisted pairs of enameled wire, where the electrode configuration and dimensions of the discharging air gap are similar to those occurring in the present study. The authors in [35] refer to literature that scrutinizes the value of the streamer constant, in particular, the relation $K_{St} = \ln(N_c)$, where $N_c = 10^6...10^8$ is the critical number of electrons required to initiate the streamer propagation mode of the discharge: “there is no reason apart from tradition for retaining $K_{[St]}$ equal to 18” [36] (p. 729). There thus seems to be a need for better understanding the inception criteria of PD in dielectric-barrier-type electrode configurations under inverter-type medium voltages.

In the absence of PDs (as well as transient overvoltages and significant dielectric heating), there is no premature failure observable when modulating a DC voltage with a medium-frequency pulse voltage (keeping the same peak voltage). In fact, the results indicate that the physical processes leading to insulation failure under a pure DC voltage are merely *modulated* by the varying voltage levels. As expected in such a picture, the observed lifetime under a pure DC stress is *shorter* than with additional pulse modulation (because the average electric field stress is lower, and the pulse transitions do not negatively affect insulation lifetime). Accordingly, there is no dependence of the lifetime on pulse switching frequency. Thus, under the investigated conditions, there is no empirical evidence for an additional “per pulse” degradation mechanism beyond those considered in points a. to c. In particular, within the time scales investigated in this study, there is no evidence for the potential aging mechanism (d.) based on the cyclic electromechanical force exerted (by the repetitive voltage pulses) on space charge evolving under the DC field component of the applied stress. Although space charge was not quantified within this study, its presence under the applied level of DC field stress (in excess of 400 kV mm^{-1}) is extremely likely, since space charge in PET foil has been measured at field strengths as low as 0.5 kV mm^{-1} [37].

5. Conclusions

The electrical endurance of PET insulation foil is investigated under DC-biased medium-frequency medium-voltage stress (DC + rectangular pulse). A sphere-plane electrode arrangement is employed, which takes care to eliminate transient overvoltages and excessive dielectric heating as causes of insulation failure. The following conclusions are drawn from the obtained results:

- PDIV is determined by the pulse peak-peak voltage U_p , but not significantly influenced by the applied DC bias U_{DC} ;
- While the spatial extent of the PDs is correctly predicted by the streamer criterion, the application of the “textbook value” for the streamer constant ($K_{St} = 14...18$) significantly overestimates the measured PDIV;
- Repetitive PDs erode the polymer surface (thinning of the foil) and breakdown occurs when the applied DC field exceeds the breakdown strength of the thinned foil;
- In the presence of PDs, the insulation lifetime shows a clear “per pulse” degradation, and it is typically *shorter* than under a pure DC voltage of the same peak amplitude;
- In the PD regime, the lifetime is inversely proportional to the optical PD intensity (as quantified by a near-UV camera) and scales as $f_0^{-0.65}$ with the switching frequency. The “per pulse deterioration” thus decreases with increasing f_0 ;
- In the absence of PDs, no evidence is found of a detrimental “per pulse” impact on insulation lifetime (it is observed to be independent of the switching frequency in the investigated range). The processes leading to failure under a pure DC voltage are merely modulated by the changing voltage levels introduced by the rectangular pulse train. Accordingly, the lifetime with pulse modulation is observed to be *larger* than under pure DC voltage of the same peak amplitude.

Given the practical importance of accurate predictions of the PDIV in the design process of Type I insulation systems [6], future research will focus on the determination of PDIV as a function of geometry and all relevant material parameters, as well as waveform dynamics.

Author Contributions: Conceptualization, C.M.F., J.W.K., F.K., T.G., and R.F.; methodology, R.F.; software, T.G. and R.F.; validation, R.F.; formal analysis, R.F.; investigation, R.F.; resources, C.M.F., J.W.K., F.K., T.G., and R.F.; data curation, R.F.; writing—original draft preparation, R.F.; writing—review and editing, C.M.F., J.W.K., F.K., T.G., and R.F.; visualization, R.F.; supervision, C.M.F., J.W.K., and F.K.; project administration, C.M.F., J.W.K., F.K., T.G., and R.F.; funding acquisition, C.M.F., J.W.K., and F.K.

Funding: This project was carried out within the frame of the Swiss Centre for Competence in Energy Research on the Future Swiss Electrical Infrastructure (SCCER-FURIES) with the financial support of the Swiss Innovation Agency.

Acknowledgments: We thank M. Refaey and U. Straumann for their valuable comments on the manuscript. We acknowledge the service of ScopeM (Scientific Center for Optical and Electron Microscopy) at ETH Zürich for the confocal microscopy imaging.

Conflicts of Interest: The authors declare no conflict of interest.

Abbreviations

The following abbreviations and variables are used in this manuscript:

AC		Alternating Current
DC		Direct Current
MF		Medium Frequency
MOSFET		Metal Oxide Field Effect Transistor
MV		Medium Voltage
PD		Partial Discharge
PDIV		Partial Discharge Inception Voltage
RH		Relative Humidity
TTF		Time To Failure
UV		Ultraviolet
d	m	Foil thickness (23 μm)
f_0	Hz	Switching frequency
h	$\text{W m}^{-2} \text{K}^{-1}$	Thermal interface conductance
k	$\text{W m}^{-1} \text{K}^{-1}$	Thermal conductivity
K_{St}	—	Streamer constant
ϑ	$^{\circ}\text{C}$	Temperature
ϑ_0	$^{\circ}\text{C}$	Room temperature
ε_{eff}	—	Effective dielectric permittivity
κ_{DC}	S m^{-1}	DC conductivity
τ_r	s	Pulse rise/fall time
U_p	V	Pulse jump voltage
U_{DC}	V	DC offset voltage

Appendix A. Indentation of an Elastic Insulation Foil in a Sphere-Plane Electrode Configuration

Since the elastic modulus of aluminum ($E_{\text{Alu}} \approx 70 \text{ GPa}$) is much larger than that of PET ($E_{\text{PET}} \approx 4 \text{ GPa}$), it is justified to assume the electrodes to be nonelastic. According to the Hertzian theory of elastic contact [28], a rigid sphere of radius R indents a semi-infinite elastic medium (with $E'_{\text{PET}} = E_{\text{PET}} / (1 - \nu_{\text{PET}}^2)$ and Poisson's ratio $\nu_{\text{PET}} \approx 0.38$) by

$$\delta_{\infty} = \left[\frac{3F}{4E'_{\text{PET}} \sqrt{R}} \right]^{\frac{2}{3}}, \quad (\text{A1})$$

where F is the applied contact force. The radius of the associated area of contact is given by $a_\infty = \sqrt{d_\infty R}$. Waters [29] proposed a semiempirical extension of the Hertz model to include thin sheets of elastic materials on a rigid substrate:

$$\delta = \delta_\infty \left[1 - e^{-\frac{Ad}{\sqrt{R}\delta}} \right], \quad (\text{A2})$$

where $A = 0.67$ is an empirical constant. It can be seen that correction factor becomes relevant (<0.95) when the radius of the contact area approaches 10% of the foil thickness.

The contact force consists of the spring contact force $F_c \approx 3 \text{ N}$ and the voltage-dependent electrostatic attraction F_e of the electrodes:

$$F(\delta) = F_c + F_e(\delta) = F_c + \frac{\pi\epsilon_0 R \epsilon'(0) U_{\text{DC}}^2}{d - \delta}, \quad (\text{A3})$$

where F_e is estimated on the basis of the formula for the geometric capacitance $C_0(\delta)$ (in the limit $d \ll R$) presented in [38], i.e., using “force = partial derivative of the electrostatic energy with respect to electrode separation”:

$$F_e(\delta) = \frac{1}{2} \epsilon'(0) U_{\text{DC}}^2 \frac{\partial C_0(\delta)}{\partial \delta}. \quad (\text{A4})$$

Thus, the indentation depth δ is the solution of the equation

$$\left[\frac{3F(\delta)}{4E'_{\text{PET}} \sqrt{R}} \right]^{\frac{2}{3}} \left[1 - e^{-\frac{Ad}{\sqrt{R}\delta}} \right] - \delta = 0. \quad (\text{A5})$$

For $R = 5 \text{ mm}$, $d = 23 \text{ }\mu\text{m}$, $E'_{\text{PET}} \approx 3.4 \text{ GPa}$, and $\epsilon'(0) = 3.2$, the indentation depth is numerically determined to be

$$\delta = 0.9 \text{ }\mu\text{m} \quad (\delta_\infty = 4.4 \text{ }\mu\text{m}) \quad \text{at } U_{\text{DC}} = 0, \quad (\text{A6})$$

$$\delta = 1.2 \text{ }\mu\text{m} \quad (\delta_\infty = 7.4 \text{ }\mu\text{m}) \quad \text{at } U_{\text{DC}} = 11 \text{ kV}. \quad (\text{A7})$$

The electrostatic force $F_e(1.2 \text{ }\mu\text{m}, 11 \text{ kV}) = 2.5 \text{ N}$ adds a non-negligible fraction (45%) to the total electrode force, and the associated increase of the indentation depth amounts to about 20%. Moreover, the difference between δ and δ_∞ is very substantial, indicating that considering the indentation in a semi-infinite elastic half-space (i.e., without the correction factor introduced in Equation (A2)) would be inadequate.

Appendix B. Dielectric Heating: Estimation of Upper Limit on Temperature Rise

The goal of this section is to provide an upper bound on the maximum temperature ϑ_m inside the PET foil (see Figure A1) for a specified excitation voltage $u(t)$ and given material parameters. In order to simplify the mathematical treatment, a number of approximations that overestimate ϑ_m will be used. This will provide a formalism for determining an upper bound on ϑ_m , and hence for deciding under which conditions thermal breakdown does *not* occur.

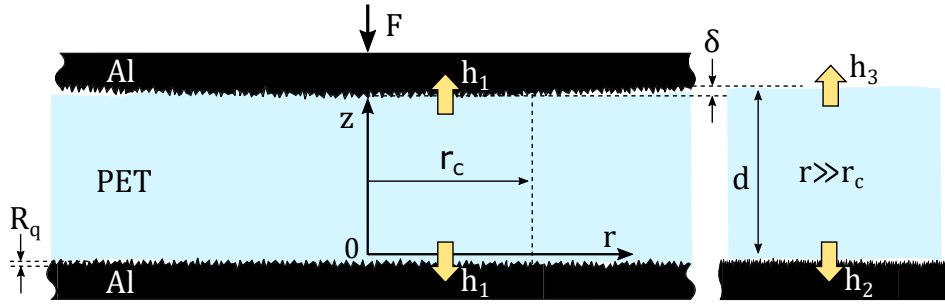


Figure A1. Enlarged view of the electrode contact area (PET foil on plane indented by half-sphere). The indented region ($r \lesssim r_c$) is shown on the left, while the right-hand side schematic depicts the area outside the indent ($r \gg r_c$). The coefficients h_1 , h_2 , and h_3 are thermal contact conductances at the respective interfaces (unit: $\text{W m}^{-2} \text{K}^{-1}$). h_1 : PET-Aluminum contact in indented region; h_2 : cooling of foil surface to loosely contacting electrode surface; h_3 : cooling of foil surface by natural convection.

The temperature distribution $\vartheta(r)$ inside the dielectric volume Ω is determined by the balance of the heat generation and its transfer to the environment (a heat bath of temperature ϑ_0). For the considered system, the steady-state temperature distribution $\vartheta(r)$ is the solution of the boundary value problem

$$-\nabla \cdot [k_{\text{PET}} \nabla \vartheta(\mathbf{r})] = \dot{q}(\mathbf{r}) \quad \forall \mathbf{r} \in \Omega, \tag{A8}$$

$$-k_{\text{PET}} \nabla \vartheta(\mathbf{r}) \cdot \mathbf{n}(\mathbf{r}) = h(\mathbf{r})[\vartheta(\mathbf{r}) - \vartheta_0] \quad \forall \mathbf{r} \in \partial\Omega, \tag{A9}$$

where $k_{\text{PET}} = 0.2 \text{ W m}^{-1} \text{ K}^{-1}$ is the thermal conductivity of PET, $\mathbf{n}(\mathbf{r})$ are the (outward-facing) surface normals at the insulation boundary $\partial\Omega$, and $h(\mathbf{r})$ are the thermal interface conductances. Worst-case estimates of the latter are derived based on the calculation procedures given in [39] and read

$$h_1 > 1 \text{ kW mm}^{-2} \text{ K}^{-1}, \tag{A10}$$

$$h_2 = 2.4 \text{ kW m}^{-2} \text{ K}^{-1}, \tag{A11}$$

$$h_3 = 0. \tag{A12}$$

The heat source term for $r \ll R$ is given by

$$\dot{q}(r, z) = \kappa_{\text{DC}}(\vartheta) \left[\frac{U_{\text{DC}}}{d} \right]^2 + \frac{\epsilon_0}{2} \sum_{n=0}^{\infty} \omega_n \epsilon''_{\text{eff},n}(\vartheta) \left[\frac{|\underline{U}_n|}{d + |\epsilon_n| \frac{r^2}{R}} \right]^2, \tag{A13}$$

where $|\epsilon_n|$ is set to zero because the DC component of the electric field is assumed to be expelled from the air gap by the deposition of surface charge. The problem can be simplified to a one-dimensional treatment (i.e., no significant lateral thermal coupling), if the spatial variation of the heat source \dot{q} is small on length scales

$$\iota_{\text{th}} = k_{\text{PET}} \left[\frac{d}{k_{\text{PET}}} + \frac{1}{h_2} \right] = 0.1 \text{ mm}. \tag{A14}$$

For volume elements in the foil that are apart by more than ι_{th} , the thermal coupling to the heat bath is stronger than the thermal coupling between them. This simplification will be used, as Equation (A13) satisfies this condition reasonably well, and, in any case, the resulting peak temperatures are higher than those derived with a two-dimensional analysis that includes in-plane heat fluxes. Equation (A8) can thus be solved by considering heat fluxes along the vertical (z) axis only, i.e., as a one-dimensional boundary value problem (no in-plane heat fluxes). The sought-after maximum temperature ϑ_m occurs at some position $z = \xi d$ with $0 \leq \xi \leq d$. If the local dielectric loss density $\dot{q}(r = 0, z)$ is approximated by $\dot{q}(\vartheta_m)$, the upper (u) and lower (d) foil surface temperatures read

$$\vartheta_u = \vartheta_0 + \frac{\dot{q}(\vartheta_m)(1 - \zeta)d}{h_u}, \quad (\text{A15})$$

$$\vartheta_d = \vartheta_0 + \frac{\dot{q}(\vartheta_m)\zeta d}{h_d}. \quad (\text{A16})$$

Equation (A8) can be integrated to

$$\vartheta(z) - \vartheta_m = -\frac{\dot{q}(\vartheta_m)}{2k_{\text{PET}}}(z - \zeta d)^2. \quad (\text{A17})$$

By imposing the boundary conditions at $z = d$ (A15) and $z = 0$ (A16), one obtains

$$\dot{q}(\vartheta_m) = \kappa_{\text{DC}}(\vartheta_m) \left[\frac{U_{\text{DC}}}{d} \right]^2 + \frac{\varepsilon_0}{2} \sum_{n=1}^{\infty} \omega_n \varepsilon''_{\text{eff},n}(\vartheta_m) \left[\frac{|U_n|}{d} \right]^2, \quad (\text{A18})$$

$$= (\vartheta_m - \vartheta_0) \underbrace{\left[\frac{d}{2} \left\{ \frac{\zeta}{h_u} + \frac{1 - \zeta}{h_d} + \frac{d}{2k_{\text{PET}}} [\zeta^2 + (1 - \zeta)^2] \right\} \right]^{-1}}_{\equiv \Gamma} = (\vartheta_m - \vartheta_0)\Gamma, \quad (\text{A19})$$

with

$$\zeta = \frac{1 + \frac{h_u d}{2k_{\text{PET}}}}{1 + \frac{h_u}{h_d} + \frac{h_u d}{k_{\text{PET}}}}. \quad (\text{A20})$$

The equation for finding ϑ_m thus reads

$$\dot{q}(\vartheta_m) = (\vartheta_m - \vartheta_0)\Gamma, \quad (\text{A21})$$

and can be solved iteratively:

$$\vartheta_{i+1} = \vartheta_i + \frac{\dot{q}(\vartheta_i)}{\Gamma} \quad i = 1, 2, \dots \quad (\text{A22})$$

The convergence of this iterative scheme implies the thermal stability of the sample. The higher-order corrections ($i \geq 2$) take into account the temperature-dependence of the dielectric losses (through κ_{DC} and $\varepsilon''_{\text{eff},n}$).

References

1. Huber, J.; Kolar, J. Solid-State Transformers: On the Origins and Evolution of Key Concepts. *IEEE Ind. Electron. Mag.* **2016**, *10*, 19–28. [CrossRef]
2. Rosero, J.; Ortega, J.; Aldabas, E.; Romeral, L. Moving towards a more electric aircraft. *IEEE Aerosp. Electron. Syst. Mag.* **2007**, *22*, 3–9. [CrossRef]
3. Oswald, N.; Anthony, P.; McNeill, N.; Star, B. An Experimental Investigation of the Trade-Off between Switching Losses and EMI Generation with Hard-Switched All-Si, Si-SiC and All-SiC Device Combinations. *IEEE Trans. Power Electron.* **2013**, *1*, 8885–8993. [CrossRef]
4. Bengtsson, T.; Dijkhuizen, F.; Ming, L.; Sahlen, F.; Liljestrand, L.; Bormann, D.; Papazyan, R.; Dahlgren, M. Repetitive fast voltage stresses—causes and effects. *IEEE Electr. Insul. Mag.* **2009**, *25*, 26–39. [CrossRef]
5. Cigre Working Group D1.43. Insulation degradation under fast, repetitive voltage pulses. *Techn. Brochure* **2017**, *2017*, 703.
6. IEC 60034-18-42. *Rotating Electrical Machines—Part 18-42: Partial Discharge Resistant Electrical Insulation Systems (Type II) Used in Rotating Electrical Machines Fed from Voltage Converters—Qualification Tests*; International Standard, Edition 1.0; International Electrotechnical Commission (IEC): Geneva, Switzerland, 2017.

7. Wang, P.; Cavallini, A.; Montanari, G. The influence of repetitive square wave voltage parameters on enameled wire endurance. *IEEE Trans. Dielectr. Electr. Insul.* **2014**, *21*, 1276–1284. [[CrossRef](#)]
8. Moonesan, M.; Jayaram, S.; Cherney, E. Time to failure of medium-voltage form-wound machine turn insulation stressed by unipolar square waves. *IEEE Trans. Dielectr. Electr. Insul.* **2015**, *22*, 3118–3125. [[CrossRef](#)]
9. Yin, W. Failure mechanism of winding insulations in inverter-fed motors. *IEEE Electr. Insul. Mag.* **1997**, *13*, 18–23. [[CrossRef](#)]
10. Kaufhold, M. Failure mechanism of the interturn insulation of low voltage electric machines fed by pulse controlled inverters. In Proceedings of the 1995 Conference on Electrical Insulation and Dielectric Phenomena, Virginia Beach, VA, USA, 22–25 October 1995; pp. 254–257. [[CrossRef](#)]
11. Hammarström, T.J.; Bengtsson, T.; Blennow, J.; Gubanski, S. Partial discharges in motor wires at PWM voltages of different smoothness. In Proceedings of the 2014 International Symposium on Electrical Insulating Materials, Niigata, Japan, 1–5 June 2014; pp. 184–187. [[CrossRef](#)]
12. Daugherty, R.; Wennerstrom, C. Need for industry standards for AC induction motors intended for use with adjustable-frequency controllers. *IEEE Trans. Ind. Appl.* **1991**, *27*, 1175–1185. [[CrossRef](#)]
13. Fabiani, D.; Montanari, G. The effect of voltage distortion on ageing acceleration of insulation systems under partial discharge activity. *IEEE Electr. Insul. Mag.* **2001**, *17*, 24–33. [[CrossRef](#)]
14. Koltunowicz, T.; Cavallini, A.; Djairam, D.; Montanari, G.; Smit, J. The influence of square voltage waveforms on transformer insulation break down voltage. In Proceedings of the 2011 Annual Report Conference on Electrical Insulation and Dielectric Phenomena, Cancun, Mexico, 16–19 October 2011; pp. 48–51. [[CrossRef](#)]
15. Sonerud, B.; Bengtsson, T.; Blennow, J.; Gubanski, S. Dielectric heating in insulating materials subjected to voltage waveforms with high harmonic content. *IEEE Trans. Dielectr. Electr. Insul.* **2009**, *16*, 926–933. [[CrossRef](#)]
16. Niayesh, K.; Gockenbach, E. On the aging mechanism of solid insulating materials exposed to repetitive high voltage pulses. *IEEE Trans. Dielectr. Electr. Insul.* **2014**, *21*, 304–310. [[CrossRef](#)]
17. Guillod, T.; Färber, R.; Rothmund, D.; Krismer, F.; Franck, C.M.; Kolar, J.W. Dielectric Losses in Dry-Type Insulation of Medium-Voltage Power Electronic Converters. *IEEE J. Emerg. Select. Top. Power Electron.* **2019**, [[CrossRef](#)]
18. Fabiani, D.; Montanari, G.; Cavallini, A.; Mazzanti, G. Relation between space charge accumulation and partial discharge activity in enameled wires under PWM-like voltage waveforms. *IEEE Trans. Dielectr. Electr. Insul.* **2004**, *11*, 393–405. [[CrossRef](#)]
19. Hudon, C.; Amyot, N.; Lebey, T.; Castelan, P.; Kandevar, N. Testing of low-voltage motor turn insulation intended for pulse-width modulated applications. *IEEE Trans. Dielectr. Electr. Insul.* **2000**, *7*, 783–789. [[CrossRef](#)]
20. Gao, B.; Wu, G.; He, J.; Lei, K. Investigation on aging mechanism of winding insulation used in inverter-fed traction motors. In Proceedings of the 2007 Annual Report—Conference on Electrical Insulation and Dielectric Phenomena, Vancouver, BC, Canada, 14–17 October 2007; pp. 107–111.
21. Hanley, T.; Burford, R.; Fleming, R.; Barber, K. A general review of polymeric insulation for use in HVDC cables. *IEEE Electr. Insul. Mag.* **2003**, *19*, 13–24. [[CrossRef](#)]
22. Jones, J.; Llewellyn, J.; Lewis, T. The contribution of field-induced morphological change to the electrical aging and breakdown of polyethylene. *IEEE Trans. Dielectr. Electr. Insul.* **2005**, *12*, 951–966. [[CrossRef](#)]
23. Zeller, H.; Schneider, W. Electrofracture mechanics of dielectric aging. *J. Appl. Phys.* **1984**, *56*, 455–459. [[CrossRef](#)]
24. Crine, J.; Parpal, J.; Lessard, G. A model of aging of dielectric extruded cables. In Proceedings of the 3rd International Conference on Conduction and Breakdown in Solid Dielectrics, Trondheim, Norway, 3–6 July 1989; pp. 347–351. [[CrossRef](#)]
25. Dissado, L.; Mazzanti, G.; Montanari, G. The role of trapped space charges in the electrical aging of insulating materials. *IEEE Trans. Dielectr. Electr. Insul.* **1997**, *4*, 496–506. [[CrossRef](#)]
26. Blythe, A.; Bloor, D. *Electrical Properties of Polymers*, 2nd ed.; Cambridge University Press: Cambridge, UK, 2005.
27. Yasuda, H.; Stannett, V. Permeation, solution, and diffusion of water in some high polymers. *J. Polym. Sci.* **1962**, *57*, 907–923. [[CrossRef](#)]
28. Timoshenko, S.; Goodier, J. *Theory of Elasticity*, 3rd ed.; McGraw-Hill: New York, NY, USA, 1982.

29. Waters, N. The indentation of thin rubber sheets by spherical indentors. *Br. J. Phys.* **1965**, *16*, 557–563. [[CrossRef](#)]
30. Fan, H.; Li, H. High-Frequency Transformer Isolated Bidirectional DC–DC Converter Modules with High Efficiency Over Wide Load Range for 20 kVA Solid-State Transformer. *IEEE Trans. Power Electron.* **2011**, *26*, 3599–3608. [[CrossRef](#)]
31. Montanari, G.C.; Ghinello, I.; Motori, A.; Das Gupta, D. An investigation of conduction mechanisms at high-field in PET. In Proceedings of the IEEE 1997 Annual Report Conference on Electrical Insulation and Dielectric Phenomena, Minneapolis, MN, USA, 19–22 October 1997; Volume 2, pp. 451–454.
32. Schumann, W. Über das Minimum der Durchbruchfeldstärke bei Kugelelektroden. *Electr. Eng.* **1923**, *12*, 593–608. [[CrossRef](#)]
33. Zaengl, W.; Petcharak, K. *Application of Streamer Breakdown Criterion for Inhomogeneous Fields in Dry Air and SF₆*; Gaseous Dielectrics VII; Christophorou, L.G., James, D.R., Eds.; Springer: Boston, MA, USA, 1994.
34. Kuchler, A. *High Voltage Engineering*; Springer: Berlin, Germany, 2018.
35. Lusuardi, L.; Cavallini, A.; de la Calle, M.G.; Martínez-Tarifa, J.M.; Robles, G. Insulation design of low voltage electrical motors fed by PWM inverters. *IEEE Electr. Insul. Mag.* **2019**, *35*, 7–15. [[CrossRef](#)]
36. Pedersen, A. On the electrical breakdown of gaseous dielectrics—an engineering approach. In Proceedings of the Conference on Electrical Insulation and Dielectric Phenomena, Leesburg, VA, USA, 29 October–2 November 1989; pp. 21–58. [[CrossRef](#)]
37. Neagu, E.; Dias, C. Charge injection/extraction at a metal-dielectric interface: Experimental validation. *IEEE Electr. Insul. Mag.* **2009**, *25*, 15–22. [[CrossRef](#)]
38. Crowley, J. Simple Expressions for Force and Capacitance for a Conductive Sphere near a Conductive Wall. In Proceedings of the ESA Annual Meeting on Electrostatics, Minneapolis, MN, USA, 17–19 June 2008.
39. Bahrami, M.; Yovanovich, M.; Culham, J. Thermal Joint Resistances of Nonconforming Rough Surfaces with Gas-Filled Gaps. *J. Thermophys. Heat Transf.* **2004**, *18*, 326–332. [[CrossRef](#)]



© 2019 by the authors. Licensee MDPI, Basel, Switzerland. This article is an open access article distributed under the terms and conditions of the Creative Commons Attribution (CC BY) license (<http://creativecommons.org/licenses/by/4.0/>).